Dry reforming of methane over CeO$_2$-supported Pt-Co catalysts with enhanced activity

Zhenhua Xie[a,b,c], Binhang Yan[c,d], Shyam Kattel[c], Ji Hoon Lee[b], Siyu Yao[c], Qiyuan Wu[e], Ning Rui[c], Elaine Gomez[b], Zongyuan Liu[c], Wenqian Xu[f], Li Zhang[a,*], Jingguang G. Chen[b,c,**]

[a] College of Power Engineering, Chongqing University, Chongqing, 400044, China
[b] Department of Chemical Engineering, Columbia University, New York, NY, 10027, United States
[c] Chemistry Department, Brookhaven National Laboratory, Upton, NY, 11973, United States
[d] Department of Chemical Engineering, Tsinghua University, Beijing, 100084, China
[e] Material Science and Engineering, Stony Brook University, Stony Brook, NY, 11794, United States
[f] X-ray Science Division, Advanced Photon Source, Argonne National Laboratory, Argonne, Illinois, 60439, United States

ARTICLE INFO

ABSTRACT

Dry reforming of methane provides opportunities of using CH$_4$ and CO$_2$ to produce syngas. The PtCo/CeO$_2$ bimetallic catalyst shows higher activity and H$_2$/CO ratio than the corresponding monometallic catalysts, mainly attributed to the synergistic effect of Pt-Co. Structural feature of the PtCo/CeO$_2$ catalyst was revealed by diffuse reflectance infrared Fourier transform spectroscopy (DRIFTS) of adsorbed CO and *in situ* techniques like X-ray diffraction (XRD), X-ray adsorption fine structure (XAFS) and ambient-pressure X-ray photoelectron spectroscopy (AP-XPS). Pt-Co alloy and separated Co particles co-existed in the bimetallic catalyst, whereas the former was determined as the dominant active structure with a Pt-Co-mixed-surface termination. During reaction, Pt and Co in the alloy structure nearly maintained their metallic state with slight oxygen decoration, yielding oxygen-metal site-pairs (O*-*). Combined kinetic investigations and DFT calculations reveal that the O*-modified catalytic surface of PtCo/CeO$_2$ promotes C—H bond activation with higher entropy contribution (less constraints) to compensate its higher activation barrier. Thermogravimetric analysis (TGA), transmission electron microscope (TEM) and Raman spectroscopy show that the PtCo/CeO$_2$ catalyst is resistant to coke formation as effectively as Pt/CeO$_2$ and can be easily regenerated by a mild CO$_2$ treatment.

1. Introduction

Dry reforming of methane (DRM) provides an opportunity to convert CO$_2$ with another abundant greenhouse gas, CH$_4$, to produce syngas (CO + H$_2$) for Fischer-Tropsch synthesis [1–3]. In the past two decades, supported precious metals (Rh, Ru, Ir, Pt and Pd) and non-precious metal (Ni) have been widely investigated for DRM [3–14]. Compared to precious metals, Ni-based catalysts were preferred due to the comparable catalytic activity and low cost. However, they are usually accompanied with severe coke deposition that would result in significant pressure build-up within the reactor [15]. In comparison, Co-based catalysts have drawn less attention, although it has been reported that Co/MgO, Co/TiO$_2$, and Co/Al$_2$O$_3$ also demonstrate promising catalytic performance for DRM [16].

During the DRM process, Co-based catalysts usually deactivate due to coke deposition, metal sintering, metal oxidation or formation of

inactive phase [16]. In order to enhance activity and mediate deactivation, studies have been performed to understand the effects of metal loadings [17], pretreatment conditions [18], preparation methods [19], second-metal doping effect [14,20,21], and support modification [16]. Co has a higher binding energy to oxygen than Ni [13] and thus might be deactivated by metal oxidation [17]. It has been reported that a proper tuning of the O* binding strength *via* doping a second metal (M = Ni, Ru and Pt) can significantly enhance the activity and coke-resistance *via* the Co-M interactions [14,20,21]. Moreover, compared to the corresponding parent metals, the formation of the Co-M bimetallic bond usually modifies the catalytic performance [22]. The magnetic property of Co could also make it easier to recycle the precious metals simultaneously for bimetallic catalysts. Therefore, in the present work, Pt was selected to interact with Co to form bimetallic Pt-Co catalysts to potentially enhance the catalytic performance. The choice of the oxide support is also important for enhancing the catalytic activity and

stability. CeO_2 is well known for its high oxygen release/storage capacity [23], which can promote CO_2 activation and accelerate carbon removal. Therefore, CeO_2 was chosen as the support to disperse bimetallic Pt-Co particles in the present study.

The kinetics and mechanisms of DRM have been extensively investigated. In general, different rate-determining steps (RDS) or kinetically relevant steps (KRS) may dominate or co-exist at different reaction conditions, *e.g.*, temperature, pressure and surface binding strength. Jones and Nørskov et al. combined DFT and experimental approaches to investigate methane steam reforming within a wide temperature range [13]. Their results demonstrated that both the methane dissociation step (MDS) and CO formation step (CFS) can be kinetically relevant, dominant at high and low temperatures, respectively. This is consistent with the conclusion of Wei and Iglesia that the overall reaction is kinetically controlled by methane dissociation over Ni [10], Ir [9], Pt [11], Ru [24], Rh[25] and Pd [12] within the high temperature range of 823–1073 K. The RDS or KRS may also vary with pressure, as revealed by the comprehensive micro-kinetic modeling investigation by Fan et al. [26]. They reported that the overall reforming rate is jointly controlled by MDS and CFS at low CH_4 and CO_2 partial pressures (20–400 Pa), while at high pressures (1–20 ar) the former is more enhanced and thus the latter becomes more kinetically relevant. However, in general, few studies have been performed to explore the direct comparison of DRM kinetics over bimetallic and the corresponding monometallic catalysts, especially the effect of adsorbate binding strength on the reaction kinetics.

In the present work, CeO_2-supported Pt, Co and Pt-Co catalysts were synthesized and evaluated to explore the Pt-Co synergistic effect for DRM. TPR and DRIFTS as well as EXAFS were used to characterize the Pt-Co interaction in terms of reducibility, surface termination and bimetallic bond formation. In order to investigate the Pt-Co synergistic effect on the DRM kinetics, reactant partial pressure dependency combined with measured and DFT-calculated activation barriers were studied within the range of temperatures (813–873 K) and partial pressures (0–60 kPa). In addition, the activity and stability of the PtCo/CeO_2 catalyst were evaluated within a wide range of temperature (773–1073 K) and space velocity (12–240 L/g_{cat}/h). TEM, TGA and Raman spectroscopy were used to determine the main cause for deactivation as well as the identity and structure of deposited coke. Three types of treatments were adopted to evaluate the regeneration of the PtCo/CeO_2 catalyst, *i.e.*, CO_2, air and H_2.

2. Experimental and computational methods

2.1. Catalyst preparation

All the catalysts were synthesized by the slurry phase impregnation (SPI) of CeO_2 (35-45 m^2/g, cubic, Sigma-Aldrich) with the solutions of precursors, $Pt(NH_3)_4(NO_3)_2$ (Alfa Aesar) and $Co(NO_3)_2 \cdot 6H_2O$ (Alfa Aesar), prepared by adding the necessary volume of deionized water. The bimetallic PtCo/CeO_2 catalyst was synthesized *via* co-impregnation procedure with loading amounts of 1.67 wt% Pt and 1.51 wt% Co, corresponding to a Pt/Co atomic ratio of 1:3, in order to maximize the extent of Pt-Co bimetallic bond formation [27]. For the corresponding monometallic Pt/CeO_2 and Co/CeO_2 catalysts, the metal loadings were 1.67 wt% Pt and 1.51 wt% Co, respectively. The drying and calcination procedures were the same as those described previously [28].

2.2. Catalyst characterization

2.2.1. CO chemisorption

Pulse CO chemisorption was performed in an AMI-300ip (Altamira) instrument. As-prepared catalyst (~200 mg) was pre-treated under He atmosphere (50 ml/min) at 393 K for 30 min and then cooled to 323 K. Then the sample was heated to 873 K (10 K/min) and held for 1 h in a mixture of 10% H_2 in Ar (totally 50 ml/min), and cooled down in He

(50 ml/min) for degassing before pulsing 10% CO in He (590 µL loop). The amount of chemisorbed CO was used to estimate the number of metal active sites on the catalyst with an assumption of CO/metal ratio being 1:1.

2.2.2. Temperature-programmed reduction (TPR) and hydrogenation (TPH)

The same AMI-300ip (Altamira) instrument was used for TPR, and TPH measurements. For TPR tests, as-prepared sample (~200 mg) was pre-treated with a mixture of 10% O_2 in He at 750 K for 30 min and then cooled to 323 K. TPR test was subsequently performed in a mixture of 10% H_2 in Ar (total 50 ml/min) with a heating rate of 10 K/min to 750 K. A thermal conductivity detector (TCD) was used to record the hydrogen consumption profile as a function of reduction temperature, allowing a quantitative comparison of the reducibility of active metals in different catalysts. To evaluate the activity of carbon species, similar procedures described in Ref. [29] were used for the TPH tests. 50 mg of spent catalyst was loaded and heated from 323 K to 1000 K in the mixture of 10% H_2/Ar (20 ml/min) for TPH analysis. A quadrupole mass spectrometer was used to continuously record the signals of CH_4 (m/z = 16) for TPH measurements.

2.2.3. Transmission electron microscope (TEM)

The elemental distributions of the freshly reduced and spent PtCo/CeO_2 catalysts were characterized by energy-dispersive X-ray (EDX) spectroscopy mappings, which were carried out in an FEI Talos F200X (S/TEM) with an X-FEG field emission source of brightness 1.8×10^9 A/cm^2 at 200 kV. TEM imaging was carried out with a JEM-2100 F TEM. Procedures to prepare TEM samples were described in a previous work [30].

2.2.4. Thermogravimetric analysis (TGA)

The amount and type of the coke deposited on the spent catalysts were determined by the temperature-programmed oxidation (TPO) test with TGA. Spent sample (~15 mg) was loaded and dried with N_2 (30 ml/min) at 473 K for 30 min, and subsequently heated to 1100 K under O_2 (30 ml/min) with a ramping rate of 10 K/min. The relative mass loss in the TGA profile was used to quantitatively compare the amounts of coke deposited on different spent catalysts. The positions and integral areas of the 1st-derivative thermogravimetric peaks were used to correlate with the type and amount of different carbonaceous species, respectively.

2.2.5. Raman spectroscopy

The structure of the coke deposited on the spent catalysts was characterized by a Renishaw inVia Confocal Raman microscope with a 50× objective lens. The spent samples were excited by a 532 nm laser at the range of 1000–3500 cm^{-1}. The spectral acquisition consisted of four scans with an exposure time of 10 s.

2.2.6. Diffuse reflectance infrared fourier transform spectroscopy (DRIFTS)

DRIFTS experiments following the adsorption of CO on the bimetallic and monometallic catalysts were carried out with an FTIR spectrometer (Thermo Nicolet 6700). Each sample was pretreated under a H_2/He mixture (1:3) at 673 K, after which the background spectrum was collected at room temperature. The sample was exposed to a CO/He mixture (1:3) for 30 min and then pure He for 30 min. The sample spectrum was collected (512 scans) after the He purging. Scans were taken at a resolution of 4 cm^{-1}.

2.2.7. In situ time-resolved X-ray diffraction (XRD) analysis

In situ time-resolved X-ray diffraction (XRD) measurements of different catalysts were carried out within a compact flow cell at 17 BM-B (λ = 0.24141 Å) of the Advanced Photon Source (APS) at Argonne National Laboratory. The details of the compact flow cell setup have previously been provided [30–32]. Catalyst was *in situ* reduced by a

mixture of H_2/He (Red.-1: 5/5 ml/min) with the temperature ramping from room temperature to 873 K (10 K/min) and holding for 60 min. Afterwards, the catalyst was sequentially exposed to the reaction gases (Rxn.-1: CO_2/CH_4/He = 2.5/2.5/5 ml/min for 120 min; Rxn.-2: CO_2/CH_4/He = 5/1/4 ml/min for 60 min), mixture of CO_2/He (5/5 ml/min for 60 min), mixture of H_2/He (Red.-2: 5/5 ml/min for 60 min) and reaction gases (Rxn.-3: CO_2/CH_4/He = 2.5/2.5/5 ml/min for 60 min). A residual gas analyzer (RGA) was used to give a time-resolved record for reactants and products. The two-dimensional (2D) diffraction images were continuously collected by a Perkin Elmer Amorphous Silicon detector. The 2D images were subsequently integrated by the program Fit2D [33] to obtain XRD profiles. Structural refinement was performed with Rietveld method the GSAS software [34,35].

2.2.8. In situ X-ray absorption fine structure (XAFS) analyses

XAS experiments were carried out at beam line 2-2 of the Stanford Synchrotron Radiation Lightsource (SSRL). The *in situ* Pt L_3-edge and Co K-edge XAFS spectra were collected. Approximately 50 mg of the PtCo/CeO_2 catalyst (60 − 80 mesh) was loaded into a glassy-carbon tube (3 mm in O.D.), packed with quartz wool at both sides of the sample. The sample was first reduced under a H_2/He flow (10/10 mL/min) at 873 K for 60 min., and then exposed to the reaction stream (CO_2/CH_4/He = 5/5/10 ml/min) at 873 K for 100 min. The spectra (two scans) were *in situ* collected during the reduction and reaction processes. Data processing was preformed using the IFEFFIT package. Pt and Co foils were used as standard references for EXAFS fittings.

2.2.9. Ambient-pressure X-ray photoelectron spectrum (AP-XPS) analysis

A commercial SPECS AP-XPS chamber equipped with a PHOIBOS 150 EP MCD-9 analyzer was used for XPS analysis. The Ce 3d photo-emission line was used for the energy calibration based on the strongest Ce^{4+} feature (916.7 eV). The powder sample was pressed on an aluminum plate and then loaded into the AP-XPS chamber. A 10 mTorr of H_2 was used to pretreat the sample at 823 K for 1 h. Then the samples were exposed to a mixture of CH_4 (20 mTorr) and CO_2 (20 mTorr) at the reaction temperature of 823 K. Ce 3d and Pt 4f XPS regions were collected *in situ* under the pretreatment/reaction gas environment. Signal related to Co 2p was too weak to be collected.

2.3. Catalytic performance tests

Reactions were carried out within a tubular quartz reactor (4 mm I.D.) at atmospheric pressure. The catalyst bed (∼3 cm in length) was fixed at the center of the reactor by two quartz wool plugs. The temperature of the catalyst bed was measured by a thermocouple and maintained *via* a PID feedback system. For each reaction, unless stated otherwise, the as-prepared samples (40–60 mesh) were intra- and inter-particle diluted by SiO_2 powder and acid-purified quartz (40–60 mesh) in order to exclude heat and mass transport limitations. The diluted sample was pre-treated at 873 K for 1 h with a mixture of H_2 and Ar (1:1, total 40 ml/min), and then exposed to the reactant stream at the desired temperature for 13 h to reach the pseudo-steady-state, at which time the reaction rate was used for catalytic performance comparison. The reactant mixture of CO_2, CH_4 and Ar was purged into the fixed-bed *via* mass flow controllers (Brooks 5850E) at the required flow rates and feed ratios. Ar was used to carry and dilute reactants, and meanwhile acted as an internal standard gas to correct the volume-change effect due to the high-temperature reforming reaction. In order to prevent condensation, the outlet pipe was wrapped with heating tapes (> 413 K). All the effluents were analyzed online with a gas chromatography (Agilent GC 7890B) equipped with a thermal conductivity detector (TCD) and a flame ionization detector (FID). The elemental (C, H, O) balances were within 100 ± 2% for all experiments. For the sake of control, blank reactions with only tube and tube + acid-purified quartz were tested beforehand under the same reaction conditions. The conversions of reactants were below 0.1%, indicating the negligible

contribution from the gas-phase reaction or quartz. Reaction kinetics was determined at the temperature range of 813–873 K (10 K/step) and partial pressure range of CH_4 (or CO_2) from 0.0 (or 6.25) kPa to 56.25 kPa. It should be noted that the activation barriers were measured with the method for deactivating reaction as reported in our previous work [36]. The extent of catalyst deactivation after the kinetic tests of partial pressure dependence was checked by switching the reactant stream back to the initial compositions.

Conversion (X) and turnover frequency (TOF) of species i, and H_2/CO ratio were calculated as follows:

$$X_i = \frac{[F_i]_{in} - [F_i]_{out}}{[F_i]_{in}} \times 100\% \tag{1}$$

$$TOF_i = \left| \frac{[F_i]_{in} - [F_i]_{out}}{CO_{chem} \cdot m_{catalyst}} \right| \tag{2}$$

$$\frac{H_2}{CO} = \frac{[F_{H_2}]_{out}}{[F_{CO}]_{out}} \tag{3}$$

where $[F_i]_{in}$ and $[F_i]_{out}$ are the Ar-corrected inlet and outlet molar flow rates (mole/min) of species i, respectively; CO_{chem} (µmol/g) and $m_{catalyst}$ (mg) represent the number of active sites per unit mass of catalyst and the mass of catalyst, respectively.

In order to obtain the forward TOFs of CH_4 and CO_2, approaching-to-equilibrium factor (η) was used for correction.

$$\eta_1 = \frac{[P_{CO}/P^0]^2 [P_{H_2}/P^0]^2}{[P_{CO_2}/P^0][P_{CH_4}/P^0]} \times \frac{1}{K_{eq,1}} \tag{4}$$

$$\eta_2 = \frac{[P_{CO}/P^0][P_{H_2O}/P^0]}{[P_{CO_2}/P^0][P_{H_2}/P^0]} \times \frac{1}{K_{eq,2}} \tag{5}$$

where $[P_i/P^\circ]$ is the atmospheric pressure-normalized partial pressure (dimensionless) of species i, and $K_{eq,1}$ and $K_{eq,2}$ are the equilibrium constants for the DRM and reverse water-gas shift (RWGS) reactions, respectively. η_1 was much smaller than unity with a magnitude of 10^{-5}–10^{-4}, indicating that the DRM reaction was far away from equilibrium. Thus, the forward TOF of CH_4 could be directly represented by the measured CH_4 consumption rate. In contrast, η_2 for the RWGS reaction was larger, 0.2–0.4, so the forward reaction rate of CO_2 was calculated as follows:

$$TOF_{CO_2,f} = \frac{TOF_{CO,m}}{2} + \frac{TOF_{H_2O,m}}{1 - \eta} \tag{6}$$

where $TOF_{i,f}$ and $TOF_{i,m}$ are the forward and measured TOF (min^{-1}) of species i, respectively.

The activation entropy was obtained based on statistical mechanics and transition sate theory as follows:

$$k = \frac{k_B T}{h} \exp\left(-\frac{\Delta G^{\neq}}{RT}\right) = \frac{k_B T}{h} \exp\left(\frac{\Delta S^{\neq}}{R}\right) \exp\left(-\frac{\Delta H^{\neq}}{RT}\right) \tag{7}$$

where k is the reaction constant ($TOF_{CH_4,f}/P_{CH_4}$), k_B is Boltzmann constant, h is Planck constant, $\Delta G^{\neq}$, $\Delta S^{\neq}$ and $\Delta H^{\neq}$ are the Gibbs free energy change, entropy change and enthalpy change (represented by activation barrier hereafter) from the reactant state to the transition sate.

Catalyst regenerability was evaluated after the initial 15 h reaction (time on stream) followed by three "regeneration-purging-reduction-on stream" cycles (15, 10, 60 and 360 min, respectively). The treatment method consisted of the first three procedures in each cycle, *i.e.*, treatment with regeneration gas, degassing with Ar and reduction with H_2. For the sake of clarity, it was referred to as "regeneration gas" hereafter. The spent catalysts were *in situ* regenerated by three types of treatments, *i.e.*, CO_2, air and H_2, before exposing the catalyst to the reactant stream again. Note that, for the case of H_2 treatment, the catalyst was purged with Ar for 25 min before the reduction with H_2 to achieve the same time as that used for the CO_2 and air treatments. Thus,

H_2 essentially acted as the regeneration gas during this process.

2.4. Density functional theory (DFT) calculations

Spin polarized density functional theory [37,38] calculations were performed using the Vienna *Ab-Initio* Simulation Package (VASP) code [39,40]. Projector augmented wave potentials were used to describe the core electrons with the generalized gradient approximation (GGA) [41,42] using PW91 functionals [43]. The Kohn−Sham one-electron wave functions were expanded by using a plane wave basis set with a kinetic energy cutoff of 400 eV. The Brillouin zone was sampled using a $3 \times 3 \times 1$ k-point grid in the Monkhorst−Pack scheme [44]. Ionic positions were optimized until the Hellman-Feynman force on each ion was smaller than 0.02 eV/Å.

The Pt(111) surface was modeled using a four layer 3×3 surface slab. Based on the XAFS, *in situ* XRD and AP-XPS characterizations, the bimetallic surface was modeled using a four layer 4×4 surface slab by replacing half of the Pt atoms in the top two layers with Co atoms to represent a mixed-PtCo(111) surface. It should be noted that the effect of CeO_2 was not taken into account in the DFT calculation. According to our following experiments ($Ce^{4+} \leftrightarrow Ce^{3+}$ in AP-XPS and *in situ* XRD, and nearly zero-order with respect to CO_2), CeO_2 most likely played a crucial role in CO_2 activation which is not a rate-determining step, while the subsequent reforming reactions take place on the surface of metallic particles. Given that, the difference in experimental performances between the CeO_2-supported bimetallic and monometallic catalysts during reforming is mostly associated with the metal effects, which is our interest here. A 14 Å thick vacuum was added along the direction perpendicular to the surface in the slab to avoid artificial interactions between the slab and its periodic images. During geometry optimization, the atoms in the top two layers were allowed to relax while the atoms in the bottom two layers were fixed. DFT optimized configurations for possible reaction intermediates on the Pt(111) and mixed-PtCo(111) surfaces are illustrated in Fig. S1 and Fig. S2, respectively, in the Supporting Information (SI). The binding energy (*BE*) of an adsorbate was calculated as follows:

$$BE(adsorbate) = E(slab + adsorbate) - E(slab) - E(adsorbate) \tag{8}$$

where *E(slab + adsorbate)*, *E(slab)* and *E(adsorbate)* are the total energies of the slab with adsorbate, clean slab and adsorbate species in the gas phase, respectively.

The transition state of a chemical reaction was located using the climbing image nudged elastic band (CI-NEB) method implemented in VASP [45]. The activation energy (E_a) of a chemical reaction is defined as the energy difference between the initial and transition states while the reaction energy (ΔE) is defined as the energy difference between the initial and final states.

3. Results and discussion

3.1. Structural properties of Pt-Co bimetallic catalysts

Fig. 1 and Table 1 reveal that Co/CeO_2 showed very low activity and deactivated quickly. Pt/CeO_2 showed higher conversions of CO_2 and CH_4 (11.5% and 4.5%, respectively). However, the bimetallic $PtCo/CeO_2$ catalyst significantly enhanced the conversions of CO_2 and CH_4 to 25.5% and 14.3%, respectively, much higher than the sum of that of the monometallic Pt/CeO_2 and Co/CeO_2 catalysts. The enhanced activity of the $PtCo/CeO_2$ bimetallic catalyst indicates the existence of synergistic effect between Pt and Co. To unveil the synergistic effect, various characterizations were carried out in what follows.

Fig. 2(a) demonstrates the evolution of the crystal structure of $PtCo/CeO_2$ with different treatment conditions. During reduction, two abrupt lattice expansions (Fig. S3(a) in SI) were observed at ∼380 K and 725 K, respectively. The former corresponds to the surface reduction of CeO_2, while the latter indicates the partial reduction of Ce^{4+} to

Ce^{3+} in the bulk [46]. Upon exposing to the reactant stream ($CO_2 + CH_4$), the lattice constant sharply decreased (Fig. S3(b) in SI) and CO was formed simultaneously (Fig. S4 in SI), indicating the activation of CO_2 by the partially reduced CeO_2.

To investigate the evolution of the crystal structure of the metals or metal oxides, peaks within the range of 5.2-7.0° was carefully assigned and evaluated. As shown in Fig. S5 in SI, Co_3O_4 [(311)-5.6°, (440)-9.7°] was observed in the fresh catalyst, which was subsequently reduced into CoO [(200)-6.5°, (111)-5.6°, (220)-9.2°] below the temperature of ∼382 K. As the temperature increased, the peaks of CoO became diminished after 464 K, while the peaks of metallic Co [hcp: (100)-6.3°, (002)-6.7°] appeared from the temperature of 479 K, indicating a phase transformation from CoO to Co. All the above peak positions at high temperature were located slightly left to the counterparts at room temperature (*i.e.*, standard XRD spectra in Fig. S5(b)) due to the thermal lattice expansion effect. It should be noted that a peak centered at 6.11° became noticeable with increasing temperature, quite close to that of Pt(111) (6.10°) at room temperature. However, it could not be ascribed to Pt(111) since the thermal effect would shift the peak towards left and PtO_x species should be fully reduced below 450 K as shown in TPR (Fig. S6 in SI), whereas no peak at ∼6.1° was observed until 500 K. One possible origin could be from Pt particle agglomeration during reduction. However, the EXAFS fittings (Table 2) did not show coordination number (CN) of Pt-Pt, excluding the possibility of agglomeration. Given that, it is reasonable to assign it to the Pt-Co alloy, suggesting the formation of Pt-Co alloy and the existence of separated metallic Co particles.

Spectra after different treatments were compared in Fig. 2(b). After the initial reduction (Red.-1), the peak of Pt-Co alloy remained stable at different treatment conditions. In contrast, the peak intensity of Co (111) and Co(002) decreased noticeably after being exposed to the CO_2/CH_4 mixture (1:1 or 5:1) or CO_2, indicating that Co particles could be somehow oxidized by CO_2 (or CO_2-derived species). After the second reduction (Red.-2), the Co peaks were recovered and even more intense than that after Red.-1, most likely due to the agglomeration of Co particles during H_2 reduction. However, the time-resolved RGA signals (Fig S4 in SI) show a nearly identical reforming activity for Rxn.-1 and Rxn.-3, suggesting that the separated metallic Co particles are not likely the dominant active sites for reforming. This is consistent with the TPR (Fig. S6 in SI) and flow-reactor results that Co in Co/CeO_2 was completely reduced below 873 K whereas the conversions of CH_4 and CO_2 were quite low (in Table 1). This is consistent with the recent report that Co clusters are much less effectively due to their high oxophilicities and ineffective hydrogen abstraction [14]. Thus, the Pt-Co alloy is most likely the dominant active sites in the $PtCo/CeO_2$ catalyst.

To validate that the metal components were fully reduced at 873 K, H_2-TPR tests were performed for pure CeO_2, Co/CeO_2, Pt/CeO_2 and $PtCo/CeO_2$ catalysts. The reduction peaks are shown in Fig. S6 in SI, followed with the peak assignment. Combined with the *in situ* XRD analysis, the TPR results indicated that Pt and Co in either the monometallic or bimetallic catalyst were completely reduced below 873 K. Moreover, the presence of Pt in $PtCo/CeO_2$ significantly decreased the reduction temperature of cobalt oxides from the range of 450–700 K to that below 550 K.

Fig. 3(a) and (b) show the *in situ* XANES spectra of Pt L_3-edge and Co K-edge, revealing that the active metals were reduced after H_2 pretreatment at 873 K. The *in situ* XRD and TPR results also indicated a fully reduction of active metals below 873 K. However, a comparison of the spectra of Pt and Co after reduction with those of the corresponding foils showed that Pt shifted to slightly higher energy than Pt foil and that Co showed an opposite shift to Co foil, suggesting an electron transfer from Pt to Co. During reaction, the XANES spectra of Pt L_3-edge and Co K-edge generally remained unchanged, nevertheless, with a slight shift to higher energy relative to those after reduction. The slight shift most likely resulted from the oxygen decoration on the active metals due to the exposure to reactant stream. To obtain more insights
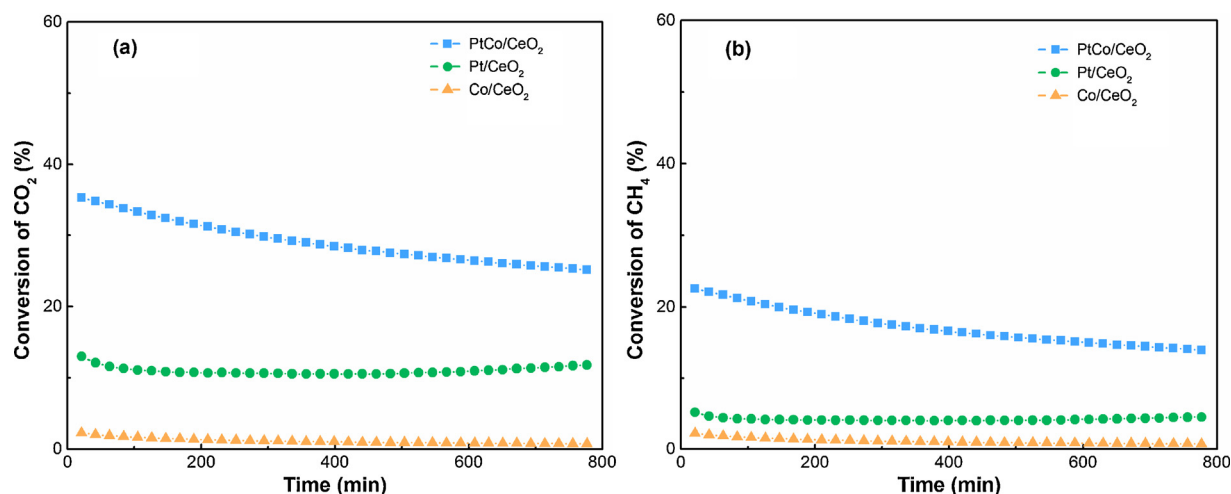
Fig. 1. Conversion of CO_2 **(a)** and CH_4 **(b)** as a function of time over $PtCo/CeO_2$, Pt/CeO_2, and Co/CeO_2 catalysts. 20 mg of pure bimetallic or monometallic catalyst with intra- and inter-particle dilution ratio of 1:5 and 1:10, respectively; 873 K, 1 atm, $CO_2/CH_4/Ar = 10/10/60$ ml/min.

Table 1
Summary of CO chemisorption and flow-reactor results for DRM reaction (20 mg of pure catalyst, $CO_2/CH_4/Ar = 10/10/60$ ml/min, 1 atm, 873 K).

Catalysts	CO chemisorption (μmol/g)	Conversion (%)		Forward TOF (mol mol_{site}^{-1} min^{-1})	
		CO_2	CH_4	CO_2	CH_4
$PtCo/CeO_2$	33.1	25.5	14.3	207.8	86.6
Pt/CeO_2	22.2	11.5	4.5	147.8	40.6
Co/CeO_2	18.1	0.8	0.8	8.3	8.3
Tube + Quartz	–	0.1	0.1	–	–
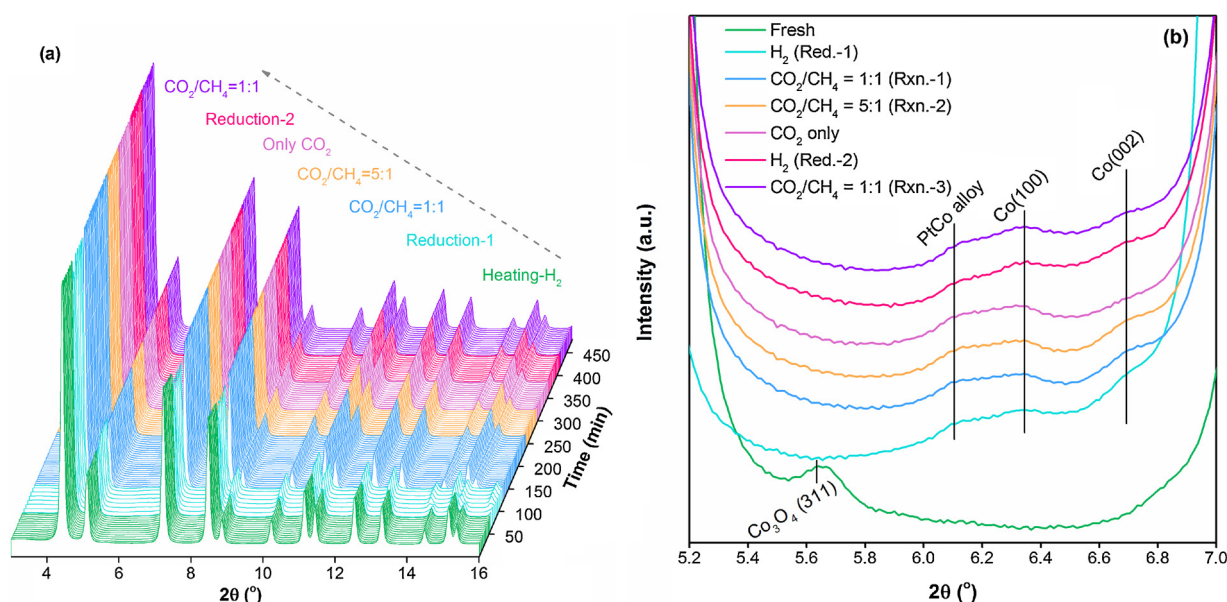
Fig. 2. Sequential XRD spectra **(a)** and evolution of XRD profiles between 5.2° and 7.0° **(b)** with different treatments: heating, reduction-1, $CO_2/CH_4 = 1:1$ (Rxn.-1), $CO_2/CH_4 = 5:1$ (Rxn.-2), CO_2 only, reduction-2, and $CO_2/CH_4 = 1:1$ (Rxn.-3).

Table 2
EXAFS fitting results of the $PtCo/CeO_2$ catalyst during reaction.

Sample	Edge	Shell	Bond length (Å)	CN	σ^2	E_0 shift
$PtCo/CeO_2$	Pt L_3	Pt-Co	2.55 ± 0.06	3.8 ± 0.6	0.008	−1.6
		Pt-Pt	–	–	–	–
	Co K	Co-Pt	–	–	–	–
		Co-Co	2.44 ± 0.01	8.0 ± 0.9	0.016	−0.3

into the specific structure of Pt and Co during reaction, EXAFS fittings (Table 2 and Fig. 3**(c)** and **(d)**) of the Pt L_3-edge and Co K-edge spectra were carried out for the $PtCo/CeO_2$ catalyst. The Pt L_3 edge EXAFS fitting results showed that the coordination number (CN) of Pt-Co was 3.8 ± 0.6 with a bond length of 2.55 ± 0.06 Å, whereas no CN of Pt-Pt could be obtained. The Co K-edge fitting results showed a Co-Co CN of 8.0 ± 0.9, however, without CN of the Co-Pt shell, suggesting the separation of large size Co particles. The EXAFS fitting results indicated
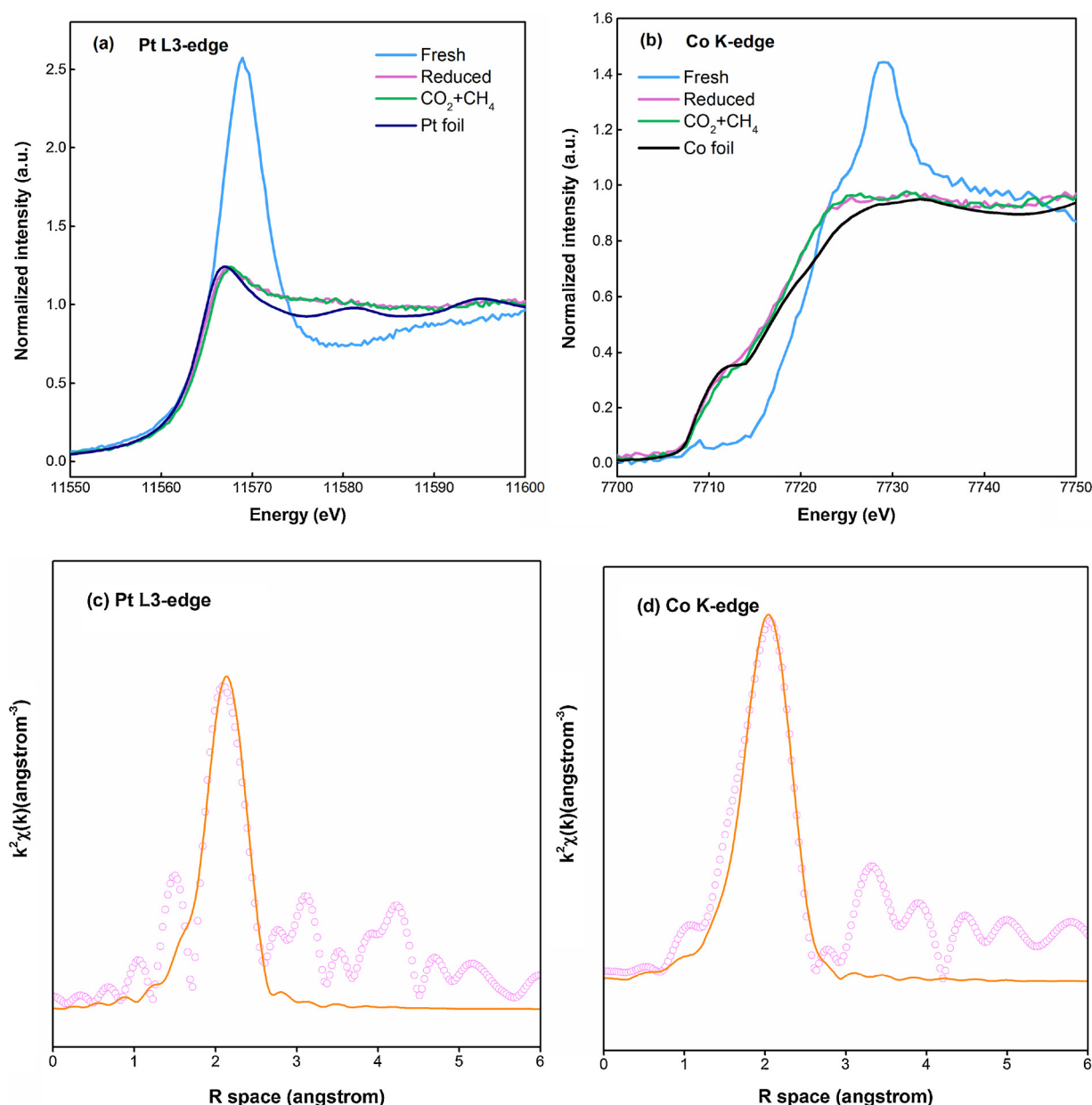
Fig. 3. *In situ* XANES spectra of Pt L$_3$-edge **(a)** and Co K-edge **(b)** of the fresh, reduced and under reaction (CO$_2$ + CH$_4$) with Pt/Co foil reference; EXAFS fitting results of Pt L$_3$-edge **(c)** and Co K-edge **(d)** in R space.

the formation of Pt-Co alloy and the existence of separated Co particles, consistent with the *in situ* XRD analysis.

In situ XRD and XAFS analyses only provided the bulk-averaged structural information. AP-XPS experiments were carried out for the PtCo/CeO$_2$ catalyst to obtain the surface information regarding the oxidation state of the catalyst during reduction and reaction. Although the TPR analysis indicated a complete reduction of Pt, Fig. 4**(a)** still showed a higher binding energy (71.6 eV) of Pt 4f$_{7/2}$ than that of metallic Pt (71.2 eV [47]), in accordance with the right shift in the Pt L$_3$-edge XANES spectrum that was induced by the electron transfer from Pt to Co. Upon exposing to the reactant stream, the Pt 4f$_{7/2}$ peak was shifted to 72.0 eV, consistent with the shift in the Pt L$_3$-edge XANES spectrum to slightly higher energy relative to that after reduction, which could be attributed to the slight oxidation of surface Pt in the presence of CO$_2$. The Co profile is not shown here due to its quite weak signal. The combination of the XANES and AP-XPS results validated the oxygen decoration on active metals of the PtCo/CeO$_2$ catalyst during reaction. Fig. 4**(b)** shows the AP-XPS profiles of Ce 3d under different

treatment conditions, in which the red peak area was used to qualitatively depict the evolution of the amount of Ce^{3+} during reduction and reaction. After reduced at 823 K, the red peaks associated with Ce^{3+} appeared, indicating the partial reduction of CeO$_2$. As the introduction of the reactants, it noticeably decreased, consistent with the time-resolved XRD results (Fig. S3(b) in SI). Thus, the reducible CeO$_2$ support should play a crucial role in CO$_2$ activation.

Fig. 5 shows the DRIFTS profiles of adsorbed CO at room temperature for freshly reduced pure CeO$_2$, PtCo/CeO$_2$, Pt/CeO$_2$ and Co/CeO$_2$ catalysts. The peaks at 2070 and 2029 cm^{-1} [48–50] over Pt/CeO$_2$ and at 2023 cm^{-1} over Co/CeO$_2$ are assigned to the linearly absorbed CO on metal atoms, while the peaks at ~1880 cm^{-1} [49,50] over both catalysts are correlated with the bridge-bound CO adsorption on metal atoms. Additional peaks were observed within the range of 1970–1930 cm^{-1} over Pt/CeO$_2$ (1965, 1956 and 1933 cm^{-1}) and Co/CeO$_2$ (1933 cm^{-1}), which most likely correspond to the CO adsorption at the metal-support interface site [49,51]. In contrast, negligible signal associated with linear CO adsorption was observed on the pure CeO$_2$
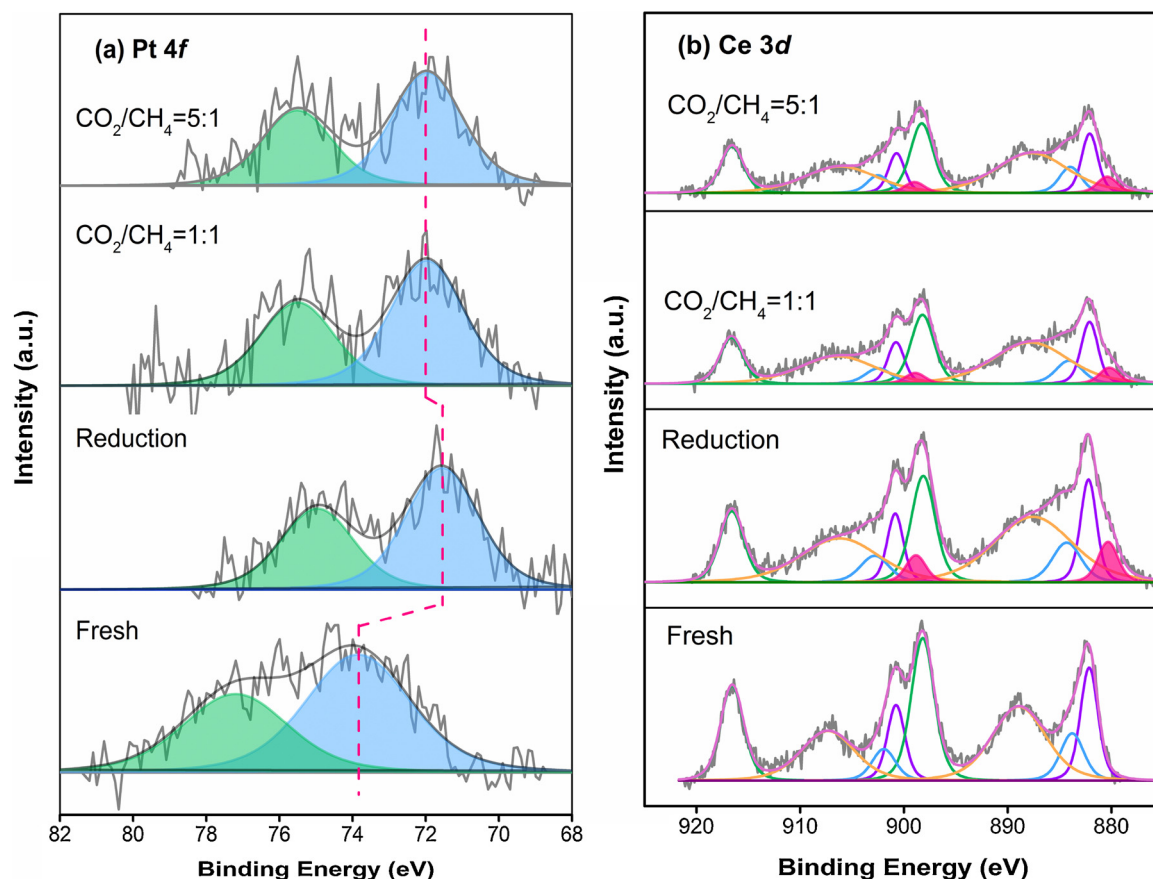
Fig. 4. AP-XPS profiles in the Pt 4f **(a)** and Ce 3d **(b)** regions of PtCo/CeO$_2$ catalyst: fresh, reduction and during reaction.
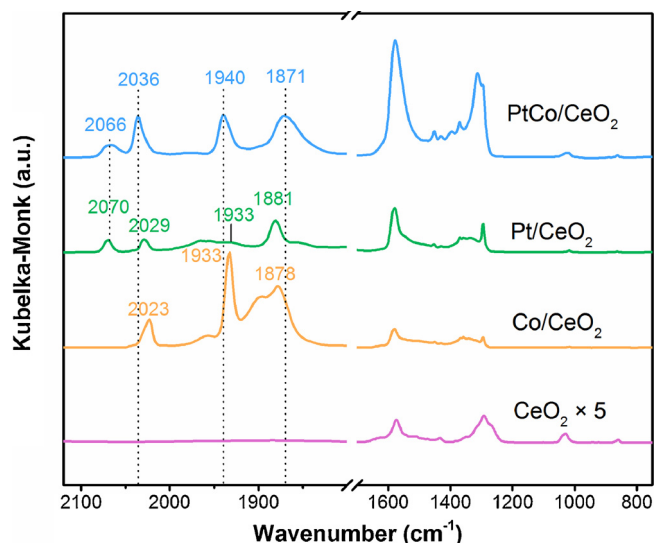

Fig. 5. DRIFTS spectra of adsorbed CO at room temperature over freshly reduced CeO$_2$, Co/CeO$_2$, Pt/CeO$_2$ and PtCo/CeO$_2$ catalysts.

within this spectral range, consistent with the previous results [52]. However, all the supported catalysts and pure CeO$_2$ presented a group of peaks within the range of 800–1650 cm^{-1}, associated with the formation of carbonate species [52], indicating that the ceria surface could be partially reduced by CO. Thus, the relatively higher peak intensity of CO could be used as an indication of more reduction of the ceria surface. By comparison, the relative peak intensity followed the disordering trend of PtCo/CeO$_2$ > Pt/CeO$_2$ > Co/CeO$_2$ > CeO$_2$, indicating that the presence of Pt and Co could promote the reduction of

CeO$_2$.

In order to determine the surface termination of the bimetallic catalyst, DRIFT spectrum of PtCo/CeO$_2$ was compared to that of Pt/CeO$_2$ and Co/CeO$_2$. A typical linear CO-Pt° peak appears at 2066 cm^{-1}, indicating the presence of Pt on the bimetallic surface. The second peak centered at 2036 cm^{-1} is due to the combined contributions from CO adsorbed on Pt and Co. The peak intensity ratio of 2036 cm^{-1} and 2066 cm^{-1} is around 3:1 on PtCo/CeO$_2$, whereas it is about 1:1 on Pt/CeO$_2$. On the other hand, the Co/CeO$_2$ surface shows a significant feature at 2023 cm^{-1}. Thus, the peak centered at 2036 cm^{-1} is assigned to the linear CO-Co° site, with additional contributions from Pt. Pt and Co in PtCo/CeO$_2$ showed a red and a blue shift relative to that of Pt/CeO$_2$ and Co/CeO$_2$, respectively, which seemed to be contradictory with the XANES and AP-XPS results (*i.e.*, electron transfer from Pt to Co). However, one could not conclusively attribute the peak shifts to electronic effects at a saturated coverage of CO, since other coverage-dependent contributions such as the dipole-dipole coupling effect and steric effect could also play a significant role [53,54]. The comparison of DRIFTS results suggests that the surface layer of the PtCo/CeO$_2$ catalyst consists of both Pt and Co.

Based on the flow-reactor experiments and characterization using *in situ* XRD, TPR, *in situ* XAFS, AP-XPS and DRIFTS, one can depict the following structural feature of the PtCo/CeO$_2$ catalyst: 1) Co forms alloy with Pt or separates as Co particles; 2) the dominant active structure is Pt-Co alloy with the co-existence of Pt and Co on the surface (*i.e.*, mixed-surface termination); and 3) during reaction, Pt and Co in the alloy structure nearly remained at their metallic state with slight oxygen decoration, yielding oxygen-metal site-pairs (O*-*) which likely play a significant role in C−H bond activation. Thus, the mixed-PtCo (111) surface structure (shown in Fig. S2 in SI) was used for the subsequent DFT calculations.
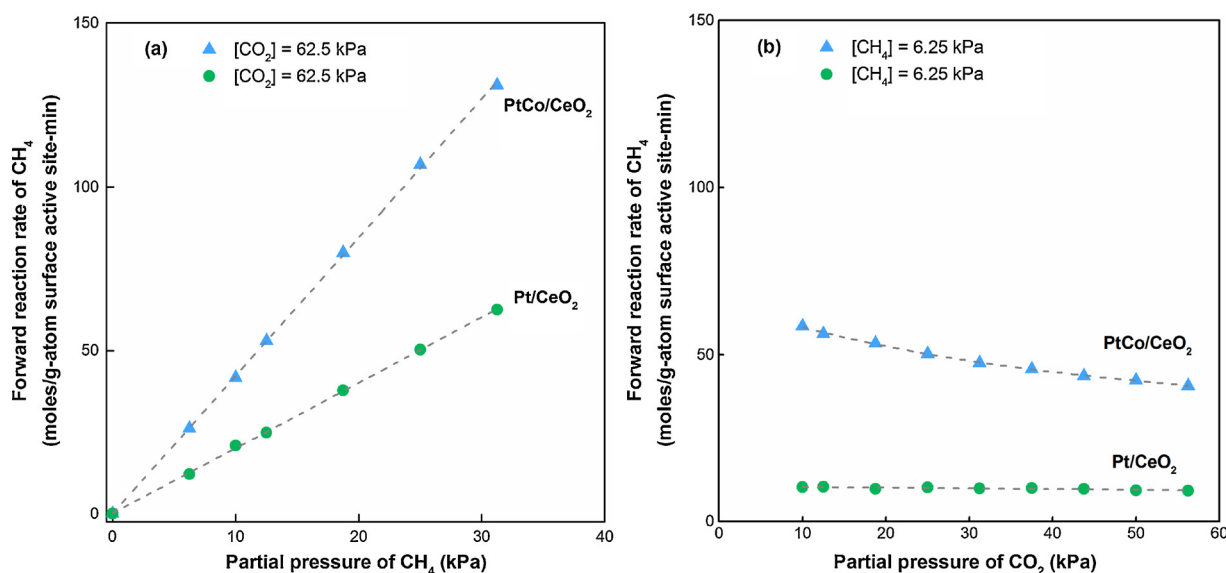
Fig. 6. Forward CH_4 reaction rate along the partial pressure of CH_4 **(a)** or CO_2 **(b)** over the $PtCo/CeO_2$ and Pt/CeO_2 catalysts at 873 K. Catalysts: $PtCo/CeO_2$ (10 mg) and Pt/CeO_2 (20 mg) with intra- and inter-particle dilution ratio of 1:5 and 1:10, respectively.

Table 3
Summary of measured apparent energy changes over the $PtCo/CeO_2$, Pt/CeO_2 and Pt/ZrO_2 catalysts.

Catalysts	Activation barrier (kJ/mol)	Activation entropy (J/mol/K)	$T\Delta S^{\neq}$ [a] (kJ/mol)	$\Delta G^{\neq}$ [a] (kJ/mol)
$PtCo/CeO_2$	123	−131	−114	237
Pt/CeO_2	111	−151	−132	243
Pt/ZrO_2	82	−187	−163	245

[a] 873 K was used for the calculation of $T\Delta S^{\neq}$ and $\Delta G^{\neq}$.

Table 4
Summary of DFT-calculated activation barriers for CO_2 and C−H bond activation in methane over the bare/O*-modified Pt(111) and mixed-PtCo(111) surfaces.

Reactions	DFT-calculated activation barriers (kJ/mol)	
	Pt(111)	Mixed-PtCo(111)
$CH_4* + * \rightarrow CH_3* + H*$	70	84
$CH_4* + O* \rightarrow CH_3* + *OH$	132	142
$CO_2* + * \rightarrow CO* + O*$	136	69

3.2. Kinetic assessment

In order to determine the synergistic or coordinated effect of Pt and Co on DRM kinetics, experiments were performed to determine the dependence on reactant partial pressures. The activation barriers were also obtained from both experimental measurements and DFT calculations.

Fig. 6**(a)** and **(b)** reveal the reactant partial pressure dependencies over the $PtCo/CeO_2$ and Pt/CeO_2 catalysts. The Co/CeO_2 catalyst was not studied due to its very low activity and fast deactivation. The measured and calculated CH_4 activation barriers are summarized in Tables 3 and 4, respectively. Fig. 7 compares the measured activation barrier plots over the $PtCo/CeO_2$, Pt/CeO_2 and Pt/ZrO_2 catalysts within the temperature range of 813–873 K. The apparent activation barriers were measured at low CH_4 conversions (below 15%) to minimize heat and mass transport limitations. Moreover, the method for measuring activation barriers of deactivating reaction was adopted to avoid the deactivation interference [36].

In the work of Wei and Iglesia [11], a linear dependence on CH_4 partial pressure and independence on CO_2 were obtained over Pt/ZrO_2 (1.6 wt%) with an apparent activation barrier for CH_4 of 83 kJ/mol. This is associated with the sole kinetic relevance of C−H bond activation on the bare Pt surface without any significant surface coverage from the CO_2-derived species. In the present work, reactant partial pressure dependencies (Fig. S7 in SI) and CH_4 activation barrier (82 kJ/mol, Table 3) over the Pt/ZrO_2 catalyst were reproduced and used as a benchmark of experimental procedures for other catalysts.

Fig. 6**(a)** and **(b)** show that, as P_{CO_2} or P_{CH_4} was maintained at the high (62.5 kPa) or low (6.25 kPa) values, the forward CH_4 reaction rate (r_{CH_4}) over Pt/CeO_2 (1.67 wt%) was proportional to P_{CH_4} and independent of P_{CO_2}, which is consistent with that in Wei and Iglesia's work over Pt/ZrO_2 [11]. However, a much higher CH_4 activation barrier (111 kJ/mol) was measured over Pt/CeO_2 than that (82 kJ/mol) over Pt/ZrO_2, most likely due to the dominance of O*-assisted activation (OA) pathway ($CH_4* + O* \rightarrow CH_3* + OH*$) rather than the direct activation (DA) route ($CH_4* + * \rightarrow CH_3* + H*$). This is consistent with the difference between the DFT-calculated activation barriers of OA (132 kJ/mol) on bare Pt(111) and DA (70 kJ/mol) on O-modified Pt (111) surfaces (Table 4).

It has been well documented that CeO_2 with its high oxygen storage/release capacity is widely used as a promoter or support to enhance CO_2 activation *via* the redox behavior of Ce^{3+}/Ce^{4+} [55–59], consistent with our findings from the *in situ* XRD and AP-XPS experiment. The CO_2-CeO_2 interaction would become significant in the case of reducible supports with a dual-site mechanism for CH_4 and CO_2 activations [3]. In addition, recent literatures [60–62] report that oxygen could easily transfer from CeO_2 onto the metal (Pt and Rh), *i.e.*, oxygen spillover, which in turn forms the metal-O species. Therefore, the reducible CeO_2 support could be responsible for promoting the OA pathway for CH_4 activation over the Pt/CeO_2 catalyst.

As for $PtCo/CeO_2$, the forward CH_4 reaction rate also increased linearly with P_{CH_4}, but it decreased gradually with increasing P_{CO_2}, which is different from that of Pt/CeO_2 or Pt/ZrO_2. The inhibition effect regarding P_{CO_2} might result from catalyst deactivation or competitive occupancy of active sites by the CO_2-derived species. The former is unlikely to be the main reason since only 8% deactivation was observed after the consecutive kinetics tests. Thus, the latter should be mainly responsible for the decreasing trend, which suggests that active sites of $PtCo/CeO_2$ are more readily covered by the CO_2-derived species than Pt/CeO_2.

DFT results in Table 4 show that CO_2 can be activated much more
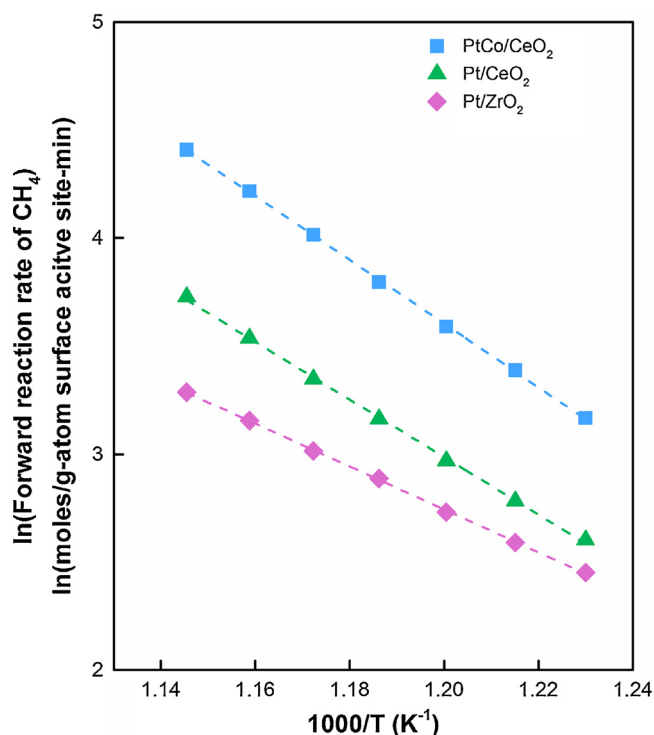
Fig. 7. Measured activation barrier plots of CH_4 over the PtCo/CeO$_2$, Pt/CeO$_2$ and Pt/ZrO$_2$ catalysts. 20 mg of pure bimetallic or monometallic catalyst with intra- and inter-particle dilution ratio of 1:5 and 1:10, respectively; 813–873 K, 1 atm, CO$_2$/CH$_4$/Ar = 10/10/60 ml/min.

Table 5
DFT calculated binding energy (in eV) of reaction intermediates derived from CH_4 and CO_2 on the Pt(111) and mixed-PtCo(111) surfaces.

Adsorbate	Pt(111)	Mixed-PtCo(111)
H	−2.79	−2.78
O	−4.19	−5.25
OH	−2.40	−3.56
CO	−1.82	−1.69
CO$_2$	−0.04	−0.13
CH$_3$	−2.15	−1.94

easily over the mixed bimetallic PtCo(111) surface (69 kJ/mol) than the Pt(111) surface (136 kJ/mol), which likely makes it possible for CO_2 to be activated both on the metal sites (competitive) and the support CeO$_2$ (non-competitive). As shown in Fig. 6(b), this is consistent with the non-typical Langmuir competitive-occupancy trend of CO_2 dependence, which decreases gradually towards a non-zero value. Moreover, as shown in Table 5, O-bound surface species, O (−5.25 *vs.* −4.19 eV) and OH (−3.56 *vs.* −2.40 eV), bind more strongly on mixed-PtCo(111) than on Pt(111), whereas other intermediates show similar binding strengths on both surfaces. The measured CH_4 activation barrier (123 kJ/mol) on PtCo/CeO$_2$ is higher than that (82 kJ/mol) on Pt/ZrO$_2$, consistent with the significant difference between the DFT calculated OA and DA barriers (142 kJ/mol *vs.* 84 kJ/mol) over the mixed-PtCo (111) surfaces. The AP-XPS experiment also pointed out the formation of Pt-O bond under reaction. Thus, it is reasonable to deduce that the PtCo/CeO$_2$ catalyst is more likely to form an O*-modified catalytic metal surface than the Pt/CeO$_2$ catalyst due to the enhanced CO_2 activation and higher O binding strength.

In general, experimentally measured kinetics combined with DFT calculations support that CH_4 is activated mainly *via* the O*-assisted mechanism over the site-pair (O*-*) of the PtCo/CeO$_2$ catalyst. It results from the O*-modified catalytic surface due to the presence of Co and reducible CeO$_2$. It has been reported that, compared with the oxidative addition step of C−H bond activation on Ni clusters, the σ bond metathesis step on NiCo and Co clusters with higher O* binding strength can yield a higher activation barrier due to the weak interaction of O* with the leaving H from CH_4(g) and weak interaction of Co with CH$_3$ fragments (induced by Coulombic repulsion between the O* and the CH$_3$ fragment) [14]. However, the weakly bound CH$_3$ fragment retains most of its gas-phase entropy and thus partially compensates the higher barrier by less entropy change at the transition state [14]. It seems to be the case for the current work. According to Eq. (7), both activation entropy and activation barrier play significant roles in determining the value of the reaction rate constant. Compared to the latter, the former represents the constraints by the catalytic surface for the degree of freedom of the transition state complex, which is usually significant for the activated adsorption processes. Table 3 reveals that higher activity could be due to the lower apparent activation Gibbs free energy ($\Delta G^{\neq}$): [PtCo/CeO$_2$ (237 kJ/mol) < Pt/CeO$_2$ (243 kJ/mol) < Pt/ZrO$_2$ (245 kJ/mol)]. This is due to the compensation from the apparent entropy contributions, $T\Delta S^{\neq}$, [PtCo/CeO$_2$ (−114 kJ/mol) > Pt/CeO$_2$ (−132 kJ/mol) > Pt/ZrO$_2$ (−163 kJ/mol)] to the activation barrier term [PtCo/CeO$_2$ (123 kJ/mol) > Pt/CeO$_2$ (111 kJ/mol) > Pt/ZrO$_2$ (82 kJ/mol)].
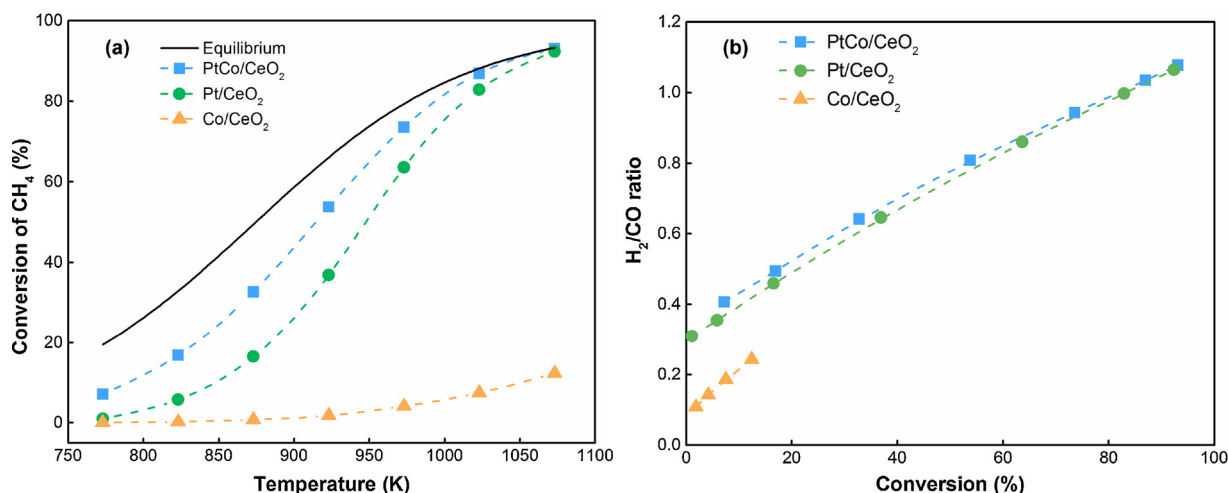

Fig. 8. Conversion of CH_4 as a function of temperature **(a)** and H$_2$/CO ratio versus conversion of CH_4 **(b)** over PtCo/CeO$_2$, Pt/CeO$_2$, and Co/CeO$_2$ catalysts. Equilibrium conversion of CH_4 represented by the solid line was calculated from HSC Chemistry 8.0 software. 100 mg of pure bimetallic or monometallic catalyst was inter-particle diluted by acid-purified quartz with a mass ratio of 1:4, 773–1073 K, 1 atm, CO$_2$/CH$_4$/Ar = 10/10/20 ml/min.
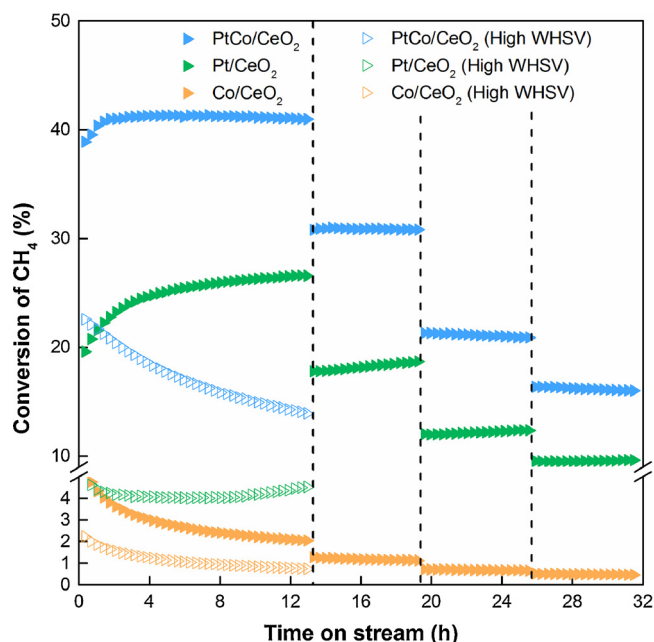
Fig. 9. Conversion of CH$_4$ as a function of time on stream at different space velocity over PtCo/CeO$_2$, Pt/CeO$_2$, and Co/CeO$_2$ catalysts. 100 mg of pure bimetallic or monometallic catalyst with an inter-particle dilution ratio of 1:5; 873 K, 1 atm; CO$_2$/CH$_4$/Ar = 5/5/10, 10/10/20, 20/20/40 and 30/30/60 ml/min. High WHSV (weight space velocity): 20 mg of pure bimetallic or monometallic catalyst with intra- and inter-particle dilution ratio of 1:5 and 1:10, respectively; 873 K, 1 atm, CO$_2$/CH$_4$/Ar = 10/10/60 ml/min.

3.3. Stability and regeneration

3.3.1. Activity and stability evaluation

Fig. 8(a) illustrates the effect of temperature on CH$_4$ conversion over the PtCo/CeO$_2$, Pt/CeO$_2$, and Co/CeO$_2$ catalysts. The "light-off" plots of Pt/CeO$_2$ and PtCo/CeO$_2$ showed a typical symmetric sigmoid shape[63], consistent with the first order with respect to P_{CH_4} as discussed in Section 3.2. Both Pt/CeO$_2$ and PtCo/CeO$_2$ showed rapid increase in CH$_4$ conversion with increasing temperature and approached the equilibrium value at high temperature (1073 K), with the latter outperforming the former during the entire temperature range. Co/CeO$_2$ was quite inactive even at high temperature (1073 K). Fig. 8(b) reveals that the H$_2$/CO ratios for the three catalysts were generally below unity but increased with the increasing temperature, indicating the presence of the concurrent RWGS reaction. The relative contribution from RWGS to the product distribution would decrease at higher DRM temperatures, consistent with the thermodynamic analysis in Ref. [3]. PtCo/CeO$_2$ and Pt/CeO$_2$ showed a similar trend of H$_2$/CO ratio along CH$_4$ conversion, implying that the difference in H$_2$/CO ratios mainly resulted from the conversion difference. Co/CeO$_2$ showed the lowest H$_2$/CO ratio (< 0.3).

As shown in Fig. 9, with the increase of space velocity by increasing flow rates or decreasing catalyst mass, CH$_4$ conversion of the three catalysts decreased. At the space velocity range of 12–72 L/g$_{cat}$/h, PtCo/CeO$_2$ showed the highest and stable CH$_4$ conversion (~42% to ~18%), followed by Pt/CeO$_2$ (~27% to ~10%). Co/CeO$_2$ still showed the lowest activity with the CH$_4$ conversion below 2.5%. In order to further evaluate the stability of different catalysts, the space velocity was significantly increased to 240 L/g$_{cat}$/h. As represented by the hollow symbols in Fig. 9, Co/CeO$_2$ was almost inactive with a CH$_4$ conversion around 1%, while Pt/CeO$_2$ maintained the CH$_4$ conversion at around 4%. Even though PtCo/CeO$_2$ showed an obvious decrease, yet around 14% of the CH$_4$ conversion was retained. In the following section, deactivation of the most active PtCo/CeO$_2$ catalyst was
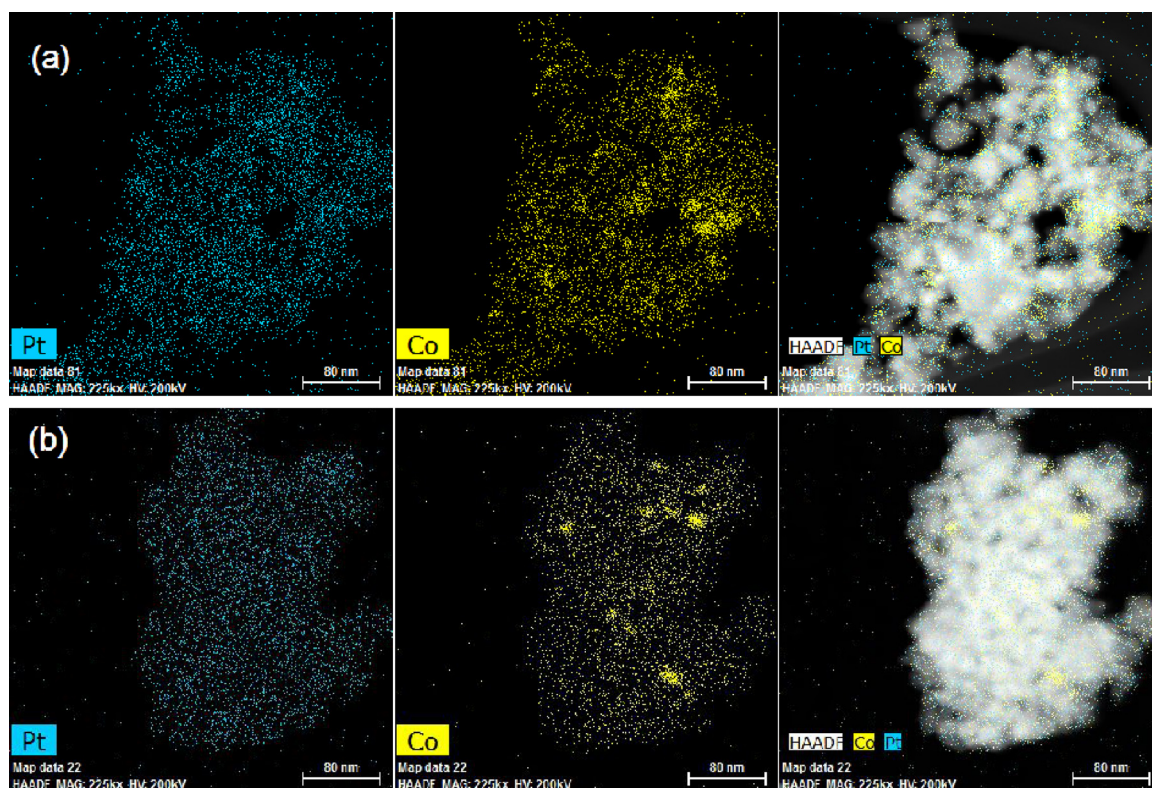

Fig. 10. EDX element mappings of reduced **(a)** and spent **(b)** PtCo/CeO$_2$ catalysts. Blue and yellow colors correspond to Pt and Co elements, respectively (For interpretation of the references to colour in this figure legend, the reader is referred to the web version of this article).
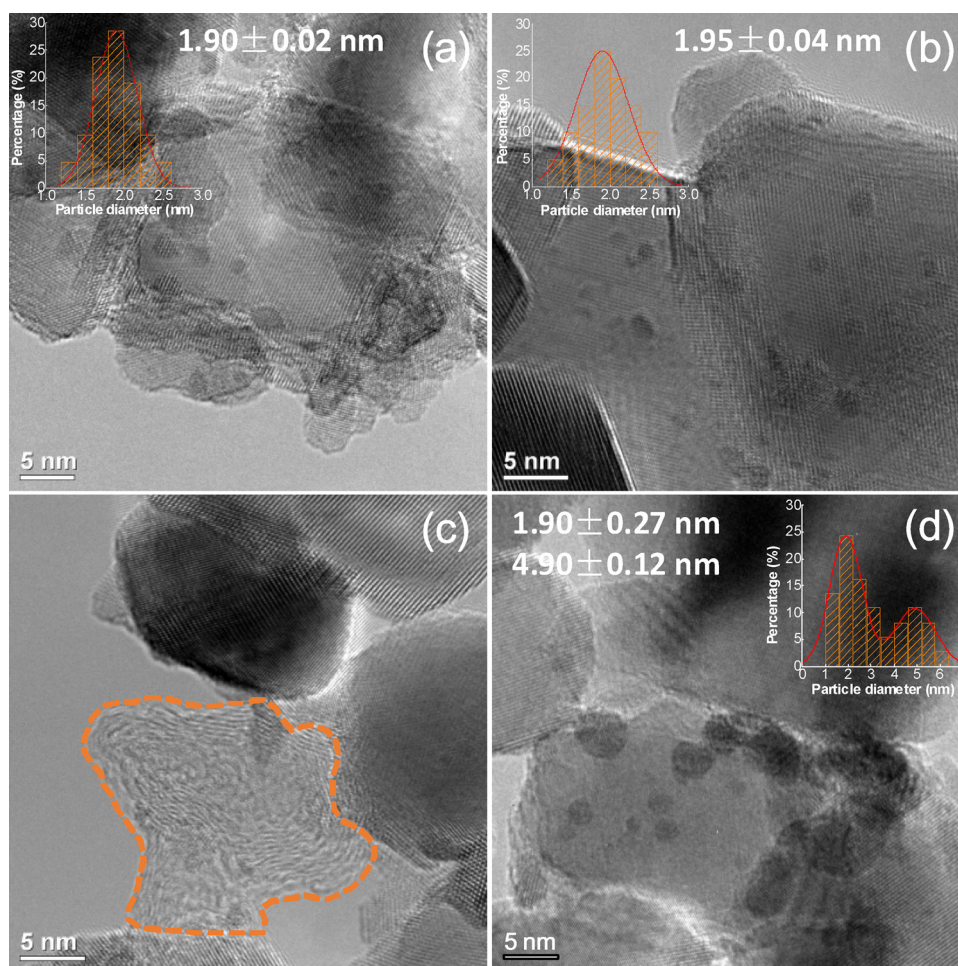
Fig. 11. TEM images of reduced **(a)**, spent **(b)**&**(c)** and regenerated **(d)** PtCo/CeO$_2$ catalyst with the metal particle size distribution. Note: figure (c) is the image of coke morphology over the spent PtCo/CeO$_2$ catalyst.

investigated using TEM, TGA and Raman spectroscopy. The regeneration of PtCo/CeO$_2$ was also evaluated with different types of treatments.

3.3.2. Deactivation and regeneration

Fig. 10 shows the elemental distributions of Pt and Co on the reduced and spent PtCo/CeO$_2$ catalysts. The active metals (Pt and Co) were generally well mixed with each other on the reduced and spent catalysts even though some agglomerations were observed. As shown in Fig. 10**(a)**, Pt was well dispersed on the reduced sample while Co showed some agglomerations, which was probably due to the H$_2$ (50% in Ar) reduction at 873 K. Fig. 10**(b)** shows that Pt was distributed uniformly on the spent catalyst. Even though Co still exhibited some agglomerations, no pronounced growth was observed compared to the freshly reduced sample. The TEM images in Fig. 11**(a)** and **(b)** also show nearly identical particle size distributions for the reduced (1.90 ± 0.02 nm) and spent (1.95 ± 0.04 nm) samples. Therefore, metal sintering is not likely the main reason to cause the deactivation of the PtCo/CeO$_2$ catalyst.

Coke deposition is a thermodynamically inevitable issue for DRM, usually considered as one of the main reasons for catalyst deactivation. TGA characterization was used to quantify the amount of coke deposited on the spent catalysts in the temperature range of 473–1100 K under an oxygen atmosphere. Fig. 12**(a)** and Table 6 illustrate that both Co/CeO$_2$ and Pt/CeO$_2$ exhibited trace amount of coke deposition (0.24% and 0.52%, respectively), for which the former was due to its quite low conversion (~1%) while the latter likely benefited from the

high coke resistance of Pt [3] and O*-modified catalytic surface. PtCo/CeO$_2$ showed a higher amount of coke deposition (1.35%), however, with the highest activity among the three catalysts. It is useful to compare the coke resistance of these three catalysts in terms of coke deposition amount per CH$_4$ conversion at steady-sate, which showed that coke resistance followed the trend of PtCo/CeO$_2$ (0.09) ≈ Pt/CeO$_2$ (0.12) > Co/CeO$_2$ (0.30). Thus, PtCo/CeO$_2$ is coke resistant, as effectively as Pt/CeO$_2$, mostly likely benefiting from its O*-modified surface discussed in section 3.2.

DTG profiles were deconvoluted by multiple Gaussian functions, as shown in Fig. 12**(b)-(d)**. This provides an opportunity to quantitatively compare the type and percentage of coke species deposited on different catalysts, as represented by T$_p$ and S$_P$ in Table 6, respectively. It is generally accepted that lower T$_p$ is related to more active carbon species, and correspondingly the types of carbon can be classified in terms of T$_p$ into amorphous carbon (473–623 K), carbon nanotubes or filamentary carbon (623–973 K) and graphitic carbon (> 923 K) [64–66]. In the present work, all three spent catalysts showed strong signals (Peak-1 and Peak-2) within 473–623 K, and weak signals (Peak-3 and Peak-4) within 623–973 K, indicating the presence of primarily amorphous carbon and carbon filaments or nanotubes. Co/CeO$_2$ and PtCo/CeO$_2$ generally exhibited a similar distribution of peak positions and corresponding percentages, except that the latter showed an additional peak at 846 K, i.e., Peak-4. Such similarity indicated that both catalysts underwent similar coke deposition process. Compared with PtCo/CeO$_2$, Pt/CeO$_2$ also showed the Peak-4 at around 761 K, whereas the former presented a slightly higher percentage (92.9%) of amorphous carbon
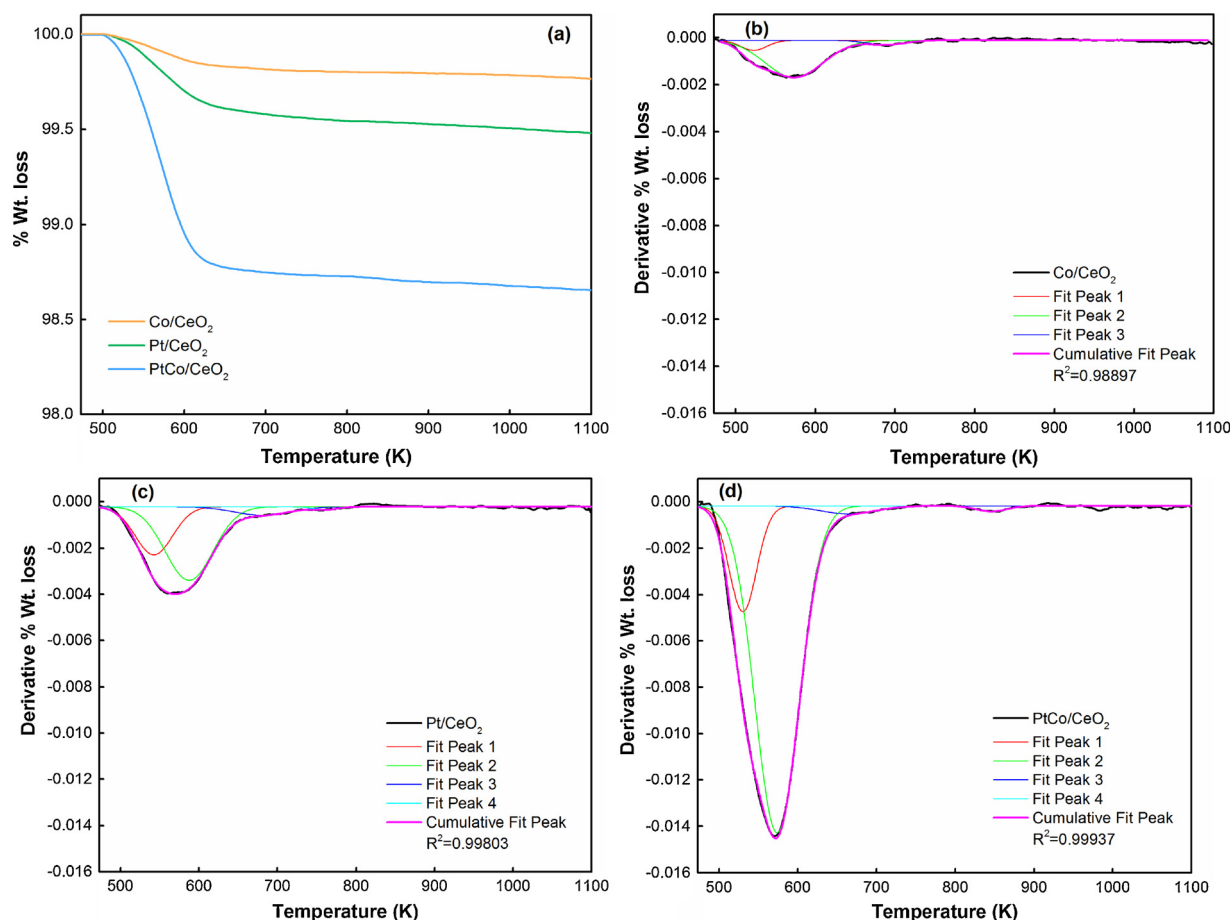
Fig. 12. TG **(a)** and DTG plots of spent Co/CeO$_2$ **(b)**, Pt/CeO$_2$ **(c)** and PtCo/CeO$_2$ **(d)** catalysts. % Wt. loss and Derivative % Wt. loss represent the weight-normalized mass loss and the first derivation of the weight-normalized mass loss to temperature, respectively.

Table 6
Summary of TGA and Raman spectroscopy results.

Catalysts	Coke amount[1] (% Wt. loss)	Coke amount[2] (% Wt. loss/CH$_4$%)	T_p^a (K) or S_p^b (%)				Total A_p^c	I_D/I_G
			Peak-1	Peak-2	Peak-3	Peak-4		
Co/CeO$_2$	0.24	0.30	523/12.2%	575/76.5%	690/11.2%	-/0.0%	0.23	1.50
Pt/CeO$_2$	0.53	0.12	543/27.8%	587/53.7%	680/14.8%	761/3.7%	0.54	0.94
PtCo/CeO$_2$	1.35	0.09	530/16.4%	573/76.5%	665/4.8%	846/2.3%	1.34	1.53

[1]and [2] correspond to the mass-normalized and mass−CH$_4$ conversion (steady-state)-normalized coke deposition amounts, respectively. [a], [b] and [c] refer to the peak positions in the DTG plots, corresponding peak areas, and the sum of peak areas, respectively.

than the latter (81.5%). The structure of the coke deposited on the spent catalysts was characterized by Raman spectroscopy. As shown in Fig. 13, PtCo/CeO$_2$ exhibited much stronger Raman spectroscopy peaks than either monometallic catalyst, consistent with the higher amount of coke deposition as revealed in the TGA results. All the spent catalysts showed three vibrational peaks centered at around 1345 and 1595 cm^{-1} in the first-order Raman spectra, corresponding to the D band and G band, respectively [67–70]. It was reported that the D band was associated with the disordered defective carbon structure that was generally correlated with the amorphous carbon (a-C) or hydrogenated amorphous carbon (a-C:H) [71], while the G band reflected the ordered and well-graphitized carbon structures [72]. Thus, both disordered and ordered carbon structures were present on the three spent catalysts. The intensity ratio of the D band and G band, I_D/I_G, is a useful parameter to qualitatively compare the fractions of disordered and ordered carbons on different catalysts [66]. Table 6 shows that Co/CeO$_2$ and PtCo/CeO$_2$ exhibited similar I_D/I_G of 1.50 and 1.53, respectively, consistent with

their similar coke distribution in the DTG analysis. In addition, the observation of I_D/I_G values greater than unity indicated the prevailing of amorphous carbon, again qualitatively agreeing with the DTG analysis, as validated by the dashed area in Fig. 11**(c)**. Compared with Co/CeO$_2$ and PtCo/CeO$_2$, Pt/CeO$_2$ exhibited a lower I_D/I_G ratio of 0.94, suggesting that more ordered carbon was formed on Pt/CeO$_2$, qualitatively consistent with the higher percentage (18.5%) of coke above 623 K as shown in Table 6.

In order to evaluate the regeneration of PtCo/CeO$_2$, the freshly reduced catalyst was first exposed to the reactant stream for 15 h, followed by the regeneration with different types of treatments (*i.e.*, H$_2$, air and CO$_2$). As shown in Fig. 14, the activity could be recovered to 87% and 86% by H$_2$ treatment within the first two regeneration cycles, while only 75% was recovered after the third regeneration cycle. In order to check the reactivity of formed carbon species towards H$_2$, TPH was performed from 323 K to 1173 K for the spent PtCo/CeO$_2$ catalyst. As shown in Fig. S8 in SI, most of the carbon species (71.4%) could be
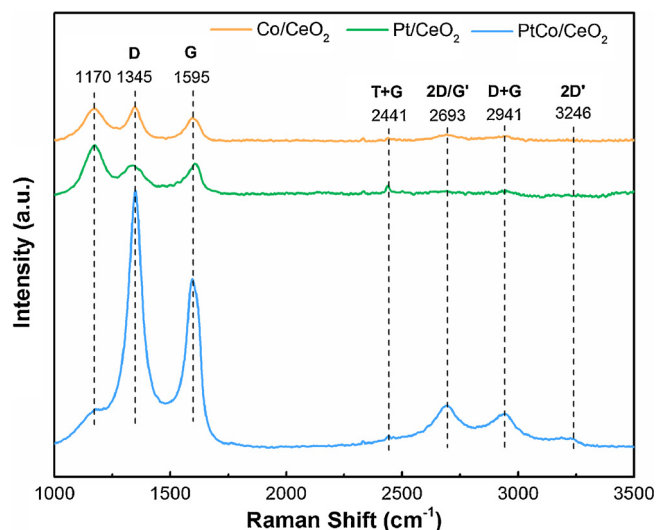
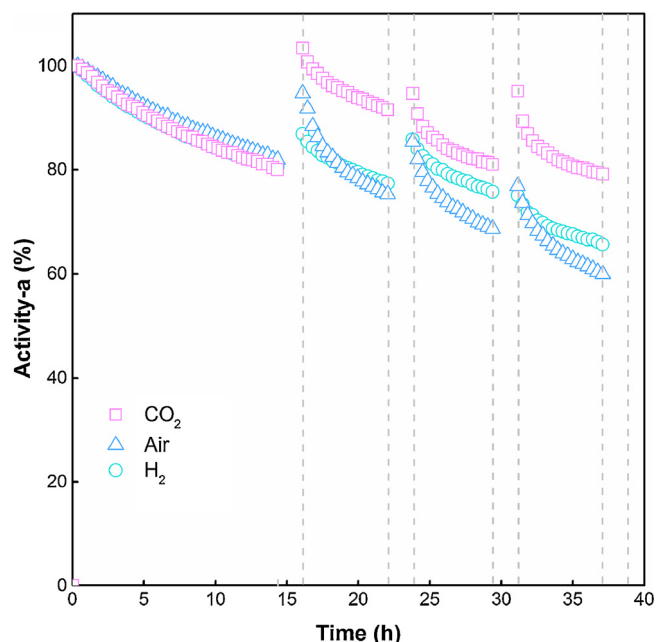**Fig. 13.** Raman spectra of spent Co/CeO₂, Pt/CeO₂ and PtCo/CeO₂ catalysts.

Fig. 14. Evaluation of activity regeneration of spent PtCo/CeO₂ catalyst with different kinds of treatments: CO₂, air and H₂. 30 mg of pure PtCo/CeO₂ with inter-particle dilution ratio of 1:4; 873 K, 1 atm, CO₂/CH₄/Ar = 10/10/60 ml/min. Regeneration: 40 ml/min of CO₂, air, or Ar for 15 min. Purging: 40 ml/min of Ar for 10 min. Reduction: 40 ml/min of H₂ and Ar with 1:1 feed ratio for 1 h.

removed by H₂ below 873 K, which contributed to the catalyst regeneration. In comparison, as the spent catalyst was regenerated by the air treatment, 95% of the activity was retained after the first regeneration cycle, benefiting from the effective coke removal by air, consistent with the TGA profile (Fig. 12(a)). However, after the second and third regeneration cycles, the initial activity dropped to 85% and 77%, respectively. In addition, the activity decreased at a higher rate than that in the initial 15 h. These results suggested that a significant irreversible inhibition effect was induced by the air treatment. The irreversible inhibition effect was most likely from the metal sintering due to the hotspot (from the exothermic coke oxidation) [73] or water vapor-induced sintering [74], since larger particles (4.90 ± 0.12 nm) appeared as shown in Fig. 11(d). Thus, mild treatment, i.e., CO₂, was utilized to help remove coke and meanwhile avoiding possible sintering, which showed that the activity could be fully recovered after the

first regeneration cycle and the deactivation rate was comparable with that in the initial 15 h. The promising regeneration results using CO₂ can be attributed to at least two factors: 1) there was no or negligible metal sintering effect during the CO₂ treatment, again supporting the main deactivation reason for PtCo/CeO₂ as coke deposition; 2) the coke deposited on PtCo/CeO₂ was in the active form that could be easily oxidized even by the mild CO₂, consistent with the high percentage of amorphous carbon at the low T_p and with the high ratio of I_D/I_G as shown in Table 6. Even though the activity was not completely recovered after the subsequent two regeneration cycles, about 95% of the initial activity was regenerated, much higher than the treatments with H₂ and air, indicating that the mild CO₂ treatment provides more effective regeneration for the spent PtCo/CeO₂ catalyst.

4. Conclusions

Based on the combined experimental and DFT results presented above, the following conclusions can be made regarding the synergistic effect of the PtCo/CeO₂ bimetallic catalyst for DRM:

1) PtCo/CeO₂ is more active with higher H₂/CO ratio than the corresponding monometallic catalysts within a wide range of temperature (773–1073 K) and space velocity (12–240 L/g_cat/h), attributed to the synergistic effect of Pt-Co bimetallic formation.

2) CeO₂ is favorable for CO₂ activation, which supplies the surface of Pt/CeO₂ with O*. The presence of Co with Pt further increases the abundance of O* by the significantly enhanced CO₂ activation as well as higher O* binding strength. The O*-modified catalytic surface of PtCo/CeO₂ promotes the reforming reaction with higher entropy contribution (less constraints) to compensate its higher activation barrier.

3) PtCo/CeO₂ gradually deactivates at the high space velocity (240 L/g_cat/h), mainly due to coke deposition instead of active metal sintering. However, it shows similar coke resistance with Pt/CeO₂. The deposited coke is mainly composed of amorphous carbon, which makes it possible to be regenerated by the mild CO₂ treatment. Other treatments with air and H₂ are less effective for regeneration.

Appendix A. Supplementary data

Supplementary material related to this article can be found, in the online version, at doi:https://doi.org/10.1016/j.apcatb.2018.05.035.

References

[1] L. Shi, G. Yang, K. Tao, Y. Yoneyama, Y. Tan, N. Tsubaki, Accounts Chem. Res. 46 (2013) 1838–1847.
[2] J.K. Dahl, A.W. Weimer, A. Lewandowski, C. Bingham, F. Bruetsch, A. Steinfeld,

Ind. Eng. Chem. Res. 43 (2004) 5489–5495.

[3] D. Pakhare, J. Spivey, Chem. Soc. Rev. 43 (2014) 7813–7837.

[4] J.R. Rostrupnielsen, J.H.B. Hansen, J. Catal. 144 (1993) 38–49.

[5] D. Qin, J. Lapszewicz, Catal. Today 21 (1994) 551–560.

[6] R. Craciun, B. Shereck, R.J. Gorte, Catal. Lett. 51 (1998) 149–153.

[7] R. Craciun, W. Daniell, H. Knözinger, Appl. Catal. A-Gen. 230 (2002) 153–168.

[8] J. Wei, E. Iglesia, Phys. Chem. Chem. Phys. 6 (2004) 3754.

[9] J. Wei, E. Iglesia, Angew. Chem. Int. Ed. 43 (2004) 3685–3688.

[10] J. Wei, E. Iglesia, J. Catal. 224 (2004) 370–383.

[11] J. Wei, E. Iglesia, J. Phys. Chem. B 108 (2004) 4094–4103.

[12] A. Yamaguchi, E. Iglesia, J. Catal. 274 (2010) 52–63.

[13] G. Jones, J.G. Jakobsen, S.S. Shim, J. Kleis, M.P. Andersson, J. Rossmeisl, F. Abild-Pedersen, T. Bligaard, S. Helveg, B. Hinnemann, J.R. Rostrup-Nielsen, I. Chorkendorff, J. Sehested, J.K. Nørskov, J. Catal. 259 (2008) 147–160.

[14] W. Tu, M. Ghoussoub, C.V. Singh, Y.-H.C. Chin, J. Am. Chem. Soc. 139 (2017) 6928–6945.

[15] Cj. Liu, J. Ye, J. Jiang, Y. Pan, ChemCatChem 3 (2011) 529–541.

[16] A.W. Budiman, S.-H. Song, T.-S. Chang, C.-H. Shin, M.-J. Choi, Catal. Surv. Asia 16 (2012) 183–197.

[17] E. Ruckenstein, H.Y. Wang, J. Catal. 205 (2002) 289–293.

[18] K. Nagaoka, Appl. Catal. A-Gen. 255 (2003) 13–21.

[19] J.L. Ewbank, L. Kovarik, C.C. Kenvin, C. Sievers, Green Chem. 16 (2014) 885–896.

[20] K. Nagaoka, Appl. Catal. A-Gen. 268 (2004) 151–158.

[21] M. Myint, B. Yan, J. Wan, S. Zhao, J.G. Chen, J. Catal. 343 (2016) 168–177.

[22] W. Yu, M.D. Porosoff, J.G. Chen, Chem. Rev. 112 (2012) 5780–5817.

[23] F. Wang, C. Li, X. Zhang, M. Wei, D.G. Evans, X. Duan, J. Catal. 329 (2015) 177–186.

[24] J. Wei, E. Iglesia, J. Phys. Chem. B 108 (2004) 7253–7262.

[25] J. Wei, E. Iglesia, J. Catal. 225 (2004) 116–127.

[26] C. Fan, Y.-A. Zhu, M.-L. Yang, Z.-J. Sui, X.-G. Zhou, D. Chen, Ind. Eng. Chem. Res. 54 (2015) 5901–5913.

[27] W.W. Lonergan, D.G. Vlachos, J.G. Chen, J. Catal. 271 (2010) 239–250.

[28] T. Wang, W. Lonergan, J.G. Chen, Chin. J. Catal. 34 (2013) 2009–2017.

[29] Y.-X. Pan, C.-J. Liu, L. Cui, Catal. Lett. 123 (2008) 96–101.

[30] B. Yan, X. Yang, S. Yao, J. Wan, M. Myint, E. Gomez, Z. Xie, S. Kattel, W. Xu, J.G. Chen, ACS Catal. 6 (2016) 7283–7292.

[31] P.J. Chupas, K.W. Chapman, C. Kurtz, J.C. Hanson, P.L. Lee, C.P. Grey, J. Appl. Crystallogr. 41 (2008) 822–824.

[32] W. Xu, R. Si, S.D. Senanayake, J. Llorca, H. Idriss, D. Stacchiola, J.C. Hanson, J.A. Rodriguez, J. Catal. 291 (2012) 117–126.

[33] A.P. Hammersley, S.O. Svensson, M. Hanfland, A.N. Fitch, D. Hausermann, High Press. Res. 14 (1996) 235–248.

[34] A.C. Larson, R.B. Von Dreele, Gsas J. (1994) 86–748 Report lAUR.

[35] B.H. Toby, J. Appl. Crystallogr. 34 (2001) 210–213.

[36] Z. Xie, B. Yan, L. Zhang, J.G. Chen, Ind. Eng. Chem. Res. 56 (2017) 1360–1364.

[37] P. Hohenberg, W. Kohn, B864, Phys. Rev. 136 (1964).

[38] W. Kohn, L.J. Sham, Phys. Rev. 140 (1965) A1133–A1138.

[39] G. Kresse, J. Furthmüller, Comp. Mater. Sci. 6 (1996) 15–50.

[40] G. Kresse, J. Hafner, Phys. Rev. B 48 (1993) 13115–13118.

[41] G. Kresse, D. Joubert, Phys. Rev. B 59 (1999) 1758–1775.

[42] P.E. Blöchl, Phys. Rev. B 50 (1994) 17953–17979.

[43] J.P. Perdew, Y. Wang, Phys. Rev. B 46 (1992) 12947–12954.

[44] H.J. Monkhorst, J.D. Pack, Phys. Rev. B 13 (1976) 5188–5192.

[45] G. Henkelman, J. Chem. Phys. 113 (2000) 9901–9904.

[46] F. Zhang, Z. Liu, S. Zhang, N. Akter, R.M. Palomino, D. Vovchok, I. Orozco, D. Salazar, J.A. Rodriguez, J. Llorca, J. Lee, D. Kim, W. Xu, A.I. Frenkel, Y. Li, T. Kim, S.D. Senanayake, ACS Catal. 8 (2018) 3550–3560.

[47] C. Wagner, Faraday Discuss. Chem. Soc. 60 (1975) 291.

[48] G. Jacobs, L. Williams, U. Graham, G.A. Thomas, D.E. Sparks, B.H. Davis, Appl. Catal. A-Gen. 252 (2003) 107–118.

[49] O. Pozdnyakova, D. Teschner, A. Wootsch, J. Kröhnert, B. Steinhauer, H. Sauer, L. Toth, F.C. Jentoft, A. Knop-Gericke, Z. Paál, R. Schlögl, J. Catal. 237 (2006) 1–16.

[50] M.J. Dees, T. Shido, Y. Iwasawa, V. Ponec, J. Catal. 124 (1990) 530–540.

[51] P. Bazin, O. Saur, J.C. Lavalley, M. Daturi, G. Blanchard, Phys. Chem. Chem. Phys. 7 (2005) 187.

[52] C. Li, Y. Sakata, T. Arai, K. Domen, K.-i. Maruya, T. Onishi, J. Chem. Soc., Faraday Trans. 1 (85) (1989) 929–943.

[53] P. Deshlahra, J. Conway, E.E. Wolf, W.F. Schneider, Langmuir 28 (2012) 8408–8417.

[54] S.C. Chang, M.J. Weaver, J. Chem. Phys. 92 (1990) 4582–4594.

[55] H.C. Yao, Y.F.Y. Yao, J. Catal. 86 (1984) 254–265.

[56] R. Wang, H. Xu, X. Liu, Q. Ge, W. Li, Appl. Catal. A: Gen. 305 (2006) 204–210.

[57] T. Jin, Y. Zhou, G.J. Mains, J.M. White, J. Phys. Chem. 91 (1987) 5931–5937.

[58] N. Laosiripojana, W. Sangtongkitcharoen, S. Assabumrungrat, Fuel 85 (2006) 323–332.

[59] T. Staudt, Y. Lykhach, N. Tsud, T. Skála, K.C. Prince, V. Matolín, J. Libuda, J. Catal. 275 (2010) 181–185.

[60] G.N. Vayssilov, Y. Lykhach, A. Migani, T. Staudt, G.P. Petrova, N. Tsud, T. Skála, A. Bruix, F. Illas, K.C. Prince, V.R. Matoĺ′n, K.M. Neyman, J. Libuda, Nat. Mater. 10 (2011) 310–315.

[61] E. Varga, P. Pusztai, L. Ovari, A. Oszko, A. Erdohelyi, C. Papp, H.P. Steinruck, Z. Konya, J. Kiss, Phys. Chem. Chem. Phys. 17 (2015) 27154–27166.

[62] A. Ruiz Puigdollers, P. Schlexer, S. Tosoni, G. Pacchioni, ACS Catal. 7 (2017) 6493–6513.

[63] F. Duprat, Chem. Eng. Sci. 57 (2002) 901–911.

[64] J.H. Lehman, M. Terrones, E. Mansfield, K.E. Hurst, V. Meunier, Carbon 49 (2011) 2581–2602.

[65] D. Bom, R. Andrews, D. Jacques, J. Anthony, B. Chen, M.S. Meier, J.P. Selegue, Nano Lett. 2 (2002) 615–619.

[66] M.H. Brijaldo, H.A. Rojas, J.J. Martínez, F.B. Passos, J. Catal. 331 (2015) 63–75.

[67] P. Tan, Y. Deng, Q. Zhao, Phys. Rev. B 58 (1998) 5435.

[68] G. Katagiri, Carbon 35 (1997) 716.

[69] Y. Kawashima, G. Katagiri, Phys. Rev. B 52 (1995) 10053.

[70] P. Tan, Y. Tang, Y.M. Deng, F. Li, Y.L. Wei, H.M. Cheng, Appl. Phys. Lett. 75 (1999) 1524–1526.

[71] J.E. Herrera, D.E. Resasco, J. Catal. 221 (2004) 354–364.

[72] Y. Kaburagi, A. Yoshida, Y. Hishiyama, F. Kang (Ed.), Materials Science and Engineering of Carbon, Butterworth-Heinemann, 2016, pp. 125–152.

[73] P. Forzatti, L. Lietti, Catal. Today 52 (1999) 165–181.

[74] G.L. Bezemer, T.J. Remans, A.P. van Bavel, A.I. Dugulan, J. Am. Chem. Soc. 132 (2010) 8540–8541.